Nanoscale Advances

ROYAL SOCIETY OF CHEMISTRY

COMMUNICATION

View Article Online
View Journal | View Issue

Cite this: *Nanoscale Adv.*, 2024, **6**, 72

Received 8th October 2023
Accepted 30th November 2023

DOI: 10.1039/d3na00867c

rsc.li/nanoscale-advances

Hollow metal–organic framework-based, stimulator of interferon genes pathway-activating nanovaccines for tumor immunotherapy†

Yilei Zhao,[a] Ruinan Song,[a] Zhen Zhang,[d] Houyang Hu,[a] Wenli Ning,[b] Xiuying Duan,[a] Jianwei Jiao,*[c] Xiao Fu*[b] and Guiqiang Zhang *[ae]

Nanovaccines have emerged as promising agents for cancer therapy because of their ability to induce specific immune responses without off-target effects. However, inadequate cytotoxic T lymphocyte response and low antigen/adjuvant encapsulation remain major obstacles to vaccinating against cancer. Herein, we designed a stimulator of interferon genes (STING) pathway-activating nanovaccine based on hollow metal–organic frameworks (MOFs) for tumor treatment. The nanovaccine (OVA@HZIF-Mn) was constructed by encapsulating a model antigen ovalbumin (OVA) into zeolitic imidazolate framework-8, followed by etching with tannic acid and functionalizing with manganese ions. Studies have shown that the nanovaccine can effectively enhance antigen uptake, STING pathway activation and dendritic cell maturation, triggering a robust immune response to inhibit tumor growth. In addition, no infection or pathological signs were observed in mice organs after multiple administrations. This study combines a simple assembly approach and superior therapeutic effect, providing a promising strategy for engineering effective nanovaccines.

Introduction

Vaccination has been regarded as one of the safest and most powerful tools to protect against various diseases because of the ability of vaccines to elicit immune responses and enable long-term immunological memory.[1,2] Vaccines can either be prophylactic, designed to prevent a future infection, or therapeutic, designed to treat an existing infection, such as cancer or bacterial infections.[3] Cancer vaccines designed to eliminate tumors have long been investigated, but only two therapeutic cancer vaccines have been approved by the U.S. Food and Drug Administration (FDA), one of which is Sipuleucel-T to treat prostate cancer.[4] Cancer vaccines typically comprise two essential components: an antigen (*e.g.*, proteins, peptides, or DNA/mRNA) and an adjuvant (a molecule or material that enhances the immunogenicity of the antigen). After administration of the vaccine (typically *via* intramuscular injection), antigen-presenting cells (APCs) ingest and internalize the vaccine *via* pattern recognition receptors on the surface of the APCs.[5] Then, APCs migrate from the local tissue through lymphatic vessels to lymph nodes (LNs), where they prime naïve T cells to effector T cells and generate immunological memory.[6] Thus, the spatiotemporal interactions between APCs and antigens (and adjuvants, if necessary) constitute a key mechanism for eliciting specific immune responses. However, some vaccines (*e.g.*, subunit vaccines) are difficult to capture and present by APCs because of their small size and metabolic instability, resulting in weak immune responses.[7]

Recently, nanovaccines, hydrogel vaccines and microvaccines have attracted significant attention in the field of tumor immunotherapy because of their excellent physicochemical properties and their ability to protect antigens from degradation.[8–11] Importantly, nanovaccines can facilitate the recruitment of antigens and adjuvants to the same APCs, thereby increasing the therapeutic efficacy of vaccines. Many nanovaccines based on liposomes, virus-like particles (VLPs), polymer nanoparticles (NPs), and inorganic NPs have been investigated, but some of these nanovaccines are often difficult to prepare and provide inadequate cytotoxic T lymphocyte response, which limits their clinical applications.[12–14] In addition, these nanovaccines suffer from poor encapsulation efficiency of antigens and adjuvants.[15] Instead, metal–organic frameworks (MOFs) represent an attractive carrier for vaccine delivery because they are trivial to prepare, have a high loading capacity, and can boast pH-sensitive degradation.[16]

Numerous studies have demonstrated that MOF-based vaccines could induce robust humoral and cellular immune

[a]*Medical Science and Technology Innovation Center, Shandong First Medical University & Shandong Academy of Medical Sciences, Jinan, Shandong 250117, China. E-mail: gqzhang2018@163.com*

[b]*School of Stomatology, Shandong First Medical University & Shandong Academy of Medical Sciences, Jinan, Shandong 250021, China. E-mail: fuxiao@sdfmu.edu.cn*

[c]*State Key Laboratory of Stem Cell and Reproductive Biology, Institute of Zoology, Chinese Academy of Science, Beijing 100101, China. E-mail: jwjiao@ioz.ac.cn*

[d]*Jinan Vocational College of Nursing, Jinan, Shandong 250102, China*

[e]*Shandong Hongkui Medical Laboratory Co., Ltd, Jinan 271100, P. R. China*

† Electronic supplementary information (ESI) available: Experimental methods and additional figures. See DOI: https://doi.org/10.1039/d3na00867c

responses and improve the stability of encapsulated antigens.[17–19] However, many of these MOFs comprise metals, such as Zr, Mg, Gd, Ni, Zn, and Cu, at high concentrations, which can pose issues with toxicity to biological systems.[20] With Zn-containing MOFs, the released Zn^{2+} might outcompete Fe^{2+} and Ca^{2+} cations for binding to macromolecular components that are necessary for cellular function, resulting in DNA damage and dysfunction of protein synthesis.[21] However, decreasing the metal content can potentially reduce the toxicity of MOFs. Caruso's group reported a top-down strategy to create voids inside MOFs using polyphenols, providing a reasonably trivial method for metal reduction.[22] Polyphenols also can endow MOFs with additional functions because they can facilitate interactions with metals, biomacromolecules, and polymers.

Emerging evidence has indicated that some metal ions play important roles in the initiation of antitumor immunity (termed metalloimmunotherapy).[23] Notably, manganese ions (Mn^{2+}) can sensitize the stimulator of interferon genes (STING) pathway to induce IFN-I secretion and subsequent immune responses.[24] However, the neurotoxicity and metabolic instability of Mn^{2+} hinder practical applications of materials containing Mn^{2+}, especially at higher concentrations.[25] Incorporating Mn^{2+} into locally injected nanovaccines as an adjuvant at low concentrations may be a promising strategy for improving their efficiency, while also enabling the co-delivery of the antigen and adjuvant. To this end, a STING pathway-activating nanovaccine (OVA@HZIF-Mn) was designed by encapsulating ovalbumin (OVA), a model antigen for immunology research, into a zeolitic imidazolate framework-8 (ZIF-8), which was then etched with tannic acid (TA) and functionalized with Mn^{2+} (Fig. 1A). We hypothesized that the hollow ZIF-8 prepared by TA etching would enhance the biosafety and OVA uptake, while the introduction of Mn^{2+} would promote STING pathway activation, and the co-delivery of Mn^{2+} and OVA would ensure they reach the same APCs. The nanovaccine was designed to improve APC uptake, activate the STING pathway, initiate robust antitumor immunity, and achieve remarkable tumor inhibition in a mouse subcutaneous melanoma tumor model (Fig. 1B).

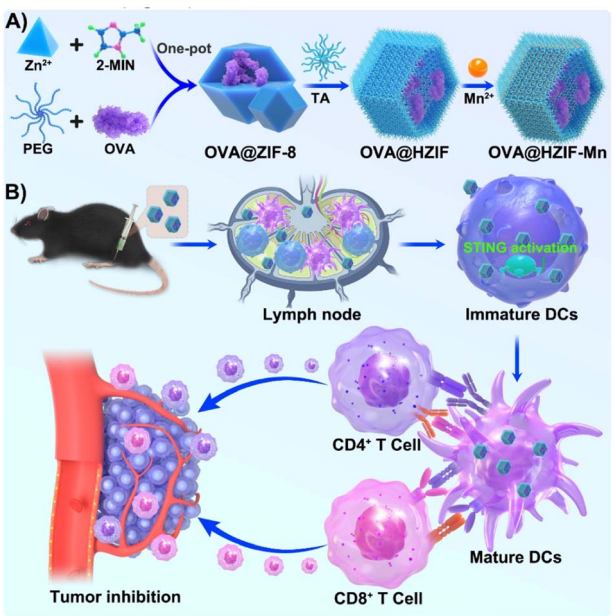

Fig. 1 Schematic illustration of (A) the preparation of the OVA@HZIF-Mn nanovaccine and (B) its function in STING pathway activation for tumor therapy.

Results and discussion

Hollow OVA@HZIF-Mn NPs were first prepared by encapsulating OVA into the ZIF-8 (OVA@ZIF) *via* a one-pot method, after which the OVA@ZIF was etched with TA (OVA@HZIF) and functionalized with Mn^{2+} ions. The morphologies and sizes of NPs were observed by TEM and SEM. As shown in Fig. 2A and S1,† OVA encapsulation, TA etching, and Mn^{2+} adsorption did not significantly change the initial shape and size compared to the unmodified ZIF-8. Remarkably low contrast was observed inside the OVA@HZIF and OVA@HZIF-Mn NPs after etching, indicating the formation of a hollow structure. Subsequently, dynamic light scattering (DLS) measurements were conducted to determine the hydrodynamic diameters of ZIF-8, OVA@ZIF, OVA@HZIF, and OVA@HZIF-Mn, which were 364.6 nm, 409.0 nm, 506.8 nm, and 509.7 nm, respectively (Fig. 2B and C). In addition, the zeta potential of ZIF-8 reversed from positive to negative after encapsulating OVA, indicating the successful loading of OVA. In addition, after etching with TA and adsorbing Mn^{2+}, the zeta potential of OVA@HZIF-Mn increased to −21.2 mV (Fig. 2D).

After storing at room temperature, the hydrodynamic diameter of the OVA@HZIF-Mn NPs in water, water containing 10% fetal bovine serum (FBS), and phosphate buffered saline

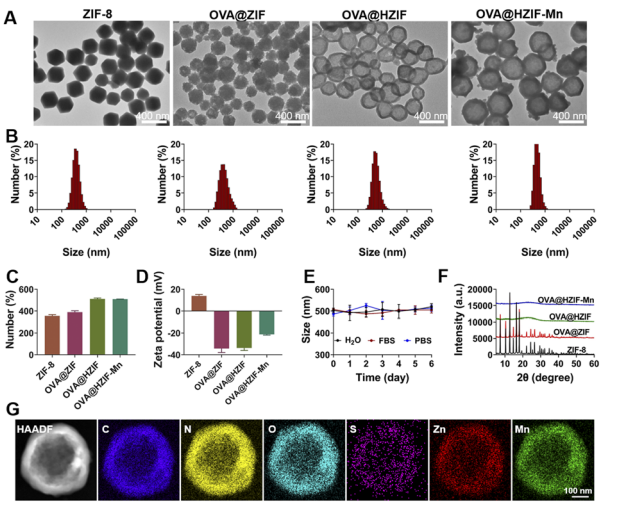

Fig. 2 (A) TEM images, (B) size distribution, (C) average sizes, and (D) zeta potential of ZIF-8, OVA@ZIF-8, OVA@HZIF and OVA@HZIF-Mn. (E) Size change of OVA@HZIF-Mn in ultrapure water, FBS, and PBS. (F) PXRD profiles of ZIF-8, OVA@ZIF-8, OVA@HZIF and OVA@HZIF-Mn. (G) HAADF-TEM and the elemental mapping images of OVA@HZIF-Mn. Scale bars are 100 nm.

(PBS) was measured by DLS every day for 6 days. The particle size did not change significantly within a week, indicating that the NPs had excellent colloidal stability (Fig. 2E). The PXRD results revealed that the crystal structure of ZIF-8 was not changed after OVA encapsulation. In contrast, after etching with TA, the diffraction peaks associated with the ZIF-8 nearly disappeared, indicating the destruction of the internal crystal structure (Fig. 2F). Inductively coupled plasma mass spectrometry (ICP-MS) assay indicated that the Zn content of ZIF-8 decreased by 31% after etching with TA. Elemental mapping images further confirmed the uniform distribution of Mn^{2+} throughout the OVA@HZIF-Mn NPs (Fig. 2G), and the loading of Mn was determined to be 9.2% using ICP-MS. Lastly, BCA assays determined that more than 75% of the OVA was encapsulated by the NPs (Fig. S2†). The successful encapsulation of OVA was also confirmed by the distribution of the S element in OVA@HZIF-Mn NPs (Fig. 2G).

The cytotoxicity of the OVA@HZIF-Mn NPs was evaluated by MTT assays. The OVA@HZIF-Mn NPs exhibited no obvious cytotoxicity even when the OVA concentration reached 90 μg mL^{-1} (viability > 85%). However, at this OVA concentration, the viability of cells treated with OVA@ZIF-8 was only 32.6% (Fig. 3A). Then, live/dead assay with propidium iodide (PI, dead cell, red) and calcein-AM (live cell, green) was used to evaluate the cytotoxicity (Fig. S3†). Increased cell death after OVA@ZIF-8 treatment was observed compared with the OVA and OVA@HZIF-Mn groups at the same concentration of OVA. Together, these results indicated that etching with TA decreased the toxicity of ZIF-8 and significantly enhanced the biocompatibility.

To assess the uptake of the antigen into cells, RAW 264.7 cells were incubated with 10 μg mL^{-1} of either FITC-OVA, FITC-OVA@ZIF or FITC-OVA@HZIF-Mn for 4 h, and analyzed by flow cytometry. The flow cytometry results showed that the FITC-positive region of the RAW 264.7 cells treated with FITC-OVA@HZIF-Mn was significantly higher than that of free FITC-OVA (Fig. 3B and C and S4†). Similarly, the flow cytometry results in DC2.4 cells also demonstrated the improved cellular internalization of FITC-OVA@HZIF-Mn (Fig. S5†). To further assess the cellular uptake of OVA, DC2.4 and RAW 264.7 cells were seeded on a cell climbing sheet and incubated with either FITC-OVA or FITC-OVA@HZIF-Mn for 4 h. Then, the cells were stained and imaged under a confocal microscope. As shown in Fig. 3D and S6,† more fluorescent-labelled OVA in FITC-OVA@HZIF-Mn was ingested into cells compared to free OVA. The localization of the antigens in the cells was investigated by confocal microscopy. In the cells treated with OVA, most of the green fluorescently labelled OVA overlapped with the red fluorescently labelled lysosomes (Fig. S7†). In contrast, partial separation of green fluorescence from red fluorescence was observed in the cells incubated with the FITC-OVA@HZIF-Mn NPs, indicating that the OVA had successfully escaped from the lysosomes.

The maturation of BMDCs is a critical step in the induction of an adaptive immune response. During this process, the expressions of pro-inflammatory cytokines and co-stimulatory markers (*e.g.*, CD80 and CD86) are significantly upregulated.[26]

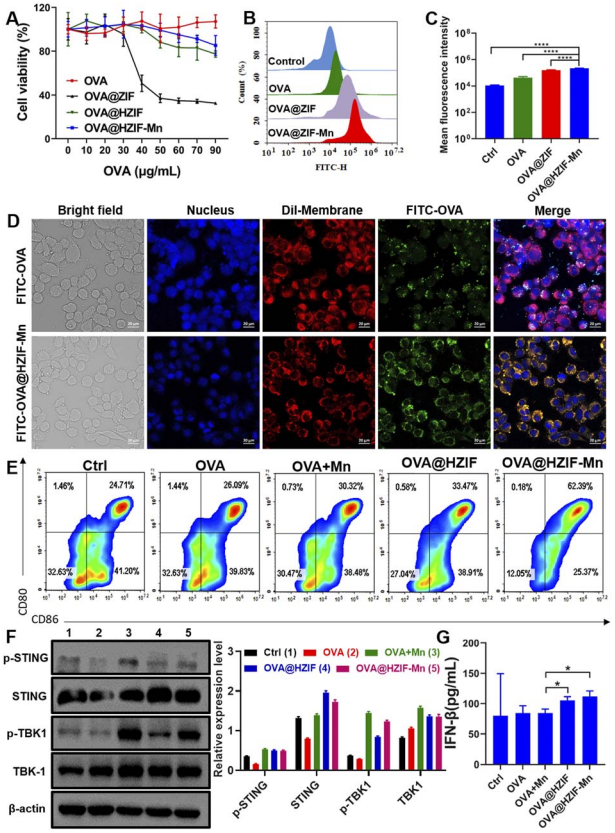

Fig. 3 (A) Cytotoxicity of OVA, OVA@ZIF8, OVA@HZIF and OVA@HZIF-Mn. Flow cytometry graphs (B) and mean fluorescence intensity (C) of cellular uptake of OVA, OVA@ZIF8, and OVA@HZIF-Mn in RAW 264.7 cells. (D) Confocal images of DC2.4 cells treated with FITC-OVA and FITC-OVA@HZIF-Mn. The nucleus and membrane were stained with DAPI (blue) and Dil (red), respectively. Scale bars are 20 μm. (E) Flow cytometry graphs of BMDCs treated with different formulations. (F) Western blot analysis of protein levels after treatment with PBS (1), OVA (2), OVA + Mn (3), OVA@HZIF (4), and OVA@HZIF-Mn (5). β-Actin was used as the loading control. (G) IFN-β secretion of BMDCs after various treatments. Data are represented as the mean ± SD ($n = 4$). *$P < 0.05$, **$P < 0.01$.

In this study, BMDCs were generated and incubated with OVA, OVA + Mn (free OVA physically mixed with Mn^{2+}), OVA@HZIF, or OVA@HZIF-Mn for 24 h. The flow cytometry results showed that treatment of the cells with OVA + Mn and OVA@HZIF only slightly increased the expression levels of the co-stimulatory markers compared to treatment with OVA ($P > 0.05$) (Fig. 3E, S8 and S9†). However, treatment of the cells with OVA@HZIF-Mn led to a significant upregulation of the expression of both CD80 and CD86 in the BMDCs compared to the other groups ($P < 0.01$).

Then, the expression levels of STING pathway-related proteins, including STING, and TBK1, were measured by western blotting. As shown in Fig. 3F and S10,† OVA@HZIF triggered phosphorylation of STING (p-STING) and TBK1 (p-TBK1) compared to the OVA group. In contrast, OVA@HZIF-Mn induced a significant increase in the levels of p-TBK1 compared to the OVA@HZIF group, indicating that it had the ability to more effectively activate the STING pathway.

Activation of the STING pathway typically upregulates the expression of type I IFNs and pro-inflammatory cytokines. The ELISA results indicated that higher levels of INF-β were detected in the cell supernatant after exposure of the cells to OVA@HZIF and OVA@HZIF-Mn, further confirming that NPs effectively activated the STING pathway (Fig. 3G).

To evaluate the antitumor effects of the NPs *in vivo*, a tumor-bearing mouse model was established by subcutaneous injection of B16F10-OVA cells into the mice. Each of the evaluated samples was injected into the tumor-bearing mice intramuscularly on day 9 and subsequently every three days for a total of four doses (Fig. 4A). Then, the tumor volumes were measured every other day during administration. As shown in Fig. 4B, the co-administration of OVA and Mn^{2+} could not produce an obvious tumor inhibition effect, while administration of the OVA@HZIF and OVA@HZIF-Mn NPs induced a significant antitumor effect over the OVA + Mn group, with the OVA@HZIF-Mn NPs eliciting a greater antitumor effect compared to the OVA@HZIF NPs ($P < 0.05$). Furthermore, the average weight and images of the excisional tumors also confirmed the excellent antitumor effect of OVA@HZIF-Mn (Fig. 4C and D). The biocompatibility of each sample was evaluated by measuring the changes in body weight, changes in the blood levels of alanine transaminase (ALT), lactate dehydrogenase (LDH), aspartate transaminase (AST), and alkaline phosphatase (ALP), and histological analysis of selected tissues in the mice during treatment with each sample. As shown in Fig. S11,† there was no significant change in body weight between the groups during treatment. In addition, levels of ALT, LDH, AST, and ALP in the serum were similar in all groups (Fig. S12†). Meanwhile, microscopy images of the H&E-stained heart, liver, lungs, kidney, and spleen tissues extracted from the mice in all groups also demonstrated the biosafety of OVA@HZIF-Mn (Fig. S13†).

To evaluate the ability of the OVA@HZIF-Mn NPs to activate the immune system, single-cell suspensions were prepared from the lymph nodes (LNs) and tumors of the immunized mice. Then, the extent of DC maturation and the proportion of $CD4^+$ T cells and $CD8^+$ T cells were quantified by flow cytometry. As shown in Fig. 4E and S14,† OVA@HZIF-Mn significantly enhanced the expression of CD80 and CD86 compared to the other groups, which was consistent with the *in vitro* DC maturation results. The flow cytometry results also showed that OVA@HZIF-Mn treatment significantly upregulated the population of $CD4^+$ and $CD8^+$ T cells in LNs (Fig. 4F, S15 and S16†). Tumor infiltration of $CD8^+$ and $CD4^+$ T cells is critical for robust tumor immunotherapy. As indicated in Fig. 4G, S17 and S18,† treatment of the mice with OVA@HZIF and OVA@HZIF-Mn elicited more $CD8^+$ and $CD4^+$ T cell infiltration in tumors compared to the other groups. Moreover, the highest frequency of $CD8^+$ infiltration into the tumor was observed after administration of the OVA@HZIF-Mn NPs to the mice, which might have been a result of activation of the STING pathway. As an index to analyze antitumor immunity, the $CD8^+/CD4^+$ ratio was also measured (Fig. S19†). Compared to other groups, the highest $CD8^+/CD4^+$ ratio was observed after administration of the OVA@HZIF-Mn NPs, further corroborating the ability of the OVA@HZIF-Mn NPs to induce a robust cellular immune response. In addition, the OVA-specific antibody IgG in serum was detected to evaluate the effect of humoral immunity. As shown in Fig. S20,† OVA@HZIF-Mn resulted in a significant increase in the IgG titer compared with other groups ($P < 0.05$ or 0.01), indicating activation of a robust humoral immune response.

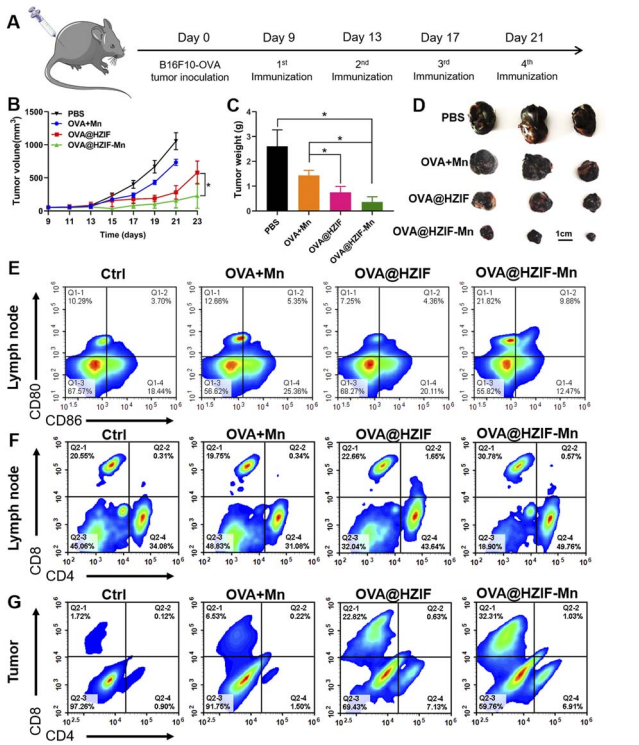

Fig. 4 (A) Schematic illustration of the experimental design. (B) The growth curves of B16-OVA tumors after administration of the samples ($n = 6$). Weights (C) and representative images (D) of harvested tumors. Flow cytometry graphs of DC maturation (E) and $CD3^+CD4^+$, $CD3^+CD8^+$ T cells (F) in LNs harvested from the immunized mice. (G) Flow cytometry graphs of $CD3^+CD4^+$ and $CD3^+CD8^+$ T cells in tumors. Data are represented as the mean ± SD ($n = 6$). *$P < 0.05$, **$P < 0.01$.

Conclusions

In summary, a STING-activating nanovaccine (OVA@HZIF-Mn) was successfully prepared through a facile method of synergistic etching and surface functionalization. The resulting OVA@HZIF-Mn exhibited a high antigen encapsulation efficiency, excellent colloidal stability, and good biocompatibility. OVA@HZIF-Mn could efficiently be taken up into APCs, and upon decomposition within the APCs, the STING pathway was activated, thereby inducing DC maturation. In a melanoma mouse model, the OVA@HZIF-Mn NPs induced an increase in tumor infiltration of effector immune cells, triggering a robust antitumor immune response that inhibited tumor growth. In addition, no infection or pathological signs were observed in the mice after multiple administrations of the nanovaccine. Overall, the nanovaccine described herein provides foundational evidence for the engineering of effective vaccines for diverse clinical applications.

Experimental section

Materials

8-arm-PEG-OH (40 kDa) was obtained from SINOPEG (China). OVA, TA, fluorescein isothiocyanate (FITC), and methylthiazolyldiphenyl-tetrazolium bromide (MTT) were purchased from Sigma-Aldrich (China). All other chemicals were purchased from Sinopharm Co., Ltd (China) unless otherwise noted. All enzyme-linked immunosorbent assay (ELISA) kits for the detection of cytokines and all fluorochrome-conjugated anti-mouse antibodies for flow cytometry were obtained from BioLegend (USA) and eBioscience (USA), respectively. The secondary antibody (Goat AntiRabbit IgG (H+L) HRP) used for WB was purchased from Shandong SparkJade Biotechnology Co., Ltd. Ultrapure water (18.2 MΩ cm) was used in all experiments.

Preparation of OVA@ZIF-8 and OVA@HZIF-Mn

To prepare the OVA@ZIF-8 NPs, 2 mL of a 160 mmol L^{-1} solution of 2-methylimidazole (2-MIM) in ultrapure water containing 8-arm-PEG-OH (10 mg) and OVA (4 mg) was mixed with 2 mL of a 40 mmol L^{-1} solution of $Zn(NO_3)_2 \cdot 6H_2O$ in ultrapure water under constant stirring at 25 °C. After 30 min, the mixture was centrifuged at 7000*g* for 5 min, and the pellet was washed three times with ultrapure water. The supernatant from the washing process was collected and the content of OVA was measured by using a bicinchoninic acid (BCA) protein assay kit. The loading rate of OVA was calculated using $(A - C \times V)/A \times 100\%$, where A is the initial amount of OVA, C is the concentration of OVA in the supernatant, and V is the volume of the supernatant.

To prepare the OVA@HZIF-Mn NPs, 1 mg of the OVA@ZIF-8 NPs was dissolved in ultrapure water, and the solution was supplemented with 50 μL of a 40 mg mL^{-1} TA solution and stirred at 25 °C for 4 h. Subsequently, the mixture was centrifuged at 7000*g* for 5 minutes, and the pellet was washed three times with ultrapure water to obtain the OVA@HZIF. Then, the pellet was added to 1 mL of a 0.06 mol L^{-1} solution of $MnCl_2$ to react overnight. Finally, the mixture was centrifuged (7000*g*, 5 min) to obtain the OVA@HZIF-Mn NPs as the pellet, which was washed with ultrapure water five times.

Characterization

Dynamic light scattering (DLS) and zeta potential measurements were performed on a Malvern Zetasizer (Nano ZS90, UK). Transmission electron microscopy (TEM, JEOL JEM-1400, Japan) and scanning electron microscope (Zeiss G300, Germany) were used to investigate the morphologies of the NPs. Powder X-ray diffraction (PXRD) patterns of the NPs were collected on an X'Pert3 Powder XRK-900 diffractometer (Anton Paar, Austria). The content of Zn and Mn encapsulated into the NPs was measured by using inductively coupled plasma mass spectrometry.

Cell culture

RAW264.7 and DC 2.4 cells were cultured in Roswell Park Memorial Institute 1640 (RPMI 1640) with 10% FBS, 1% penicillin and 1% streptomycin at 37 °C in a 5% CO_2 atmosphere.

Cytotoxicity

RAW264.7 cells were cultured in 96-well plates at a density of 10^4 cells per well in an incubator with a 5% CO_2 atmosphere at 37 °C for 24 h, to which solutions with different concentrations of OVA and OVA@HZIF-Mn were added. After 24 h, the culture medium was replaced with 100 μL of fresh medium containing 0.05 mg mL^{-1} MTT. After incubating for 4 h, 150 μL of DMSO was added to each well, and the absorbance of the solutions in each well was measured at 570 nm.

Cell uptake assays

RAW264.7 cells and DC 2.4 cells were seeded into 24-well plates at a density of 5×10^4 cells at 37 °C in a 5% CO_2 atmosphere overnight and then incubated with free OVA and OVA@HZIF-Mn at the same concentration of OVA (5 μg mL^{-1}, FITC labelled) for 4 h. Then, the cells were analyzed by confocal laser scanning microscopy (CLSM, TCP SP8 STED 3X, Germany) and flow cytometry (ACEA, NovoCyte 3009, USA).

Lysosome escape

DC 2.4 cells were seeded in 24-well plates lined with cell climbing sheets at a density of 5×10^4 cells at 37 °C in a 5% CO_2 atmosphere overnight and then incubated with free OVA and OVA@HZIF-Mn at the same concentration of OVA (5 μg mL^{-1}, FITC labelled) for 30 h. Then, the nuclei and lysosomes were stained with 4′,6-diamidino-2-phenylindole (DAPI, blue) and LysoTracker (red), respectively. The cells were analyzed by confocal laser scanning microscopy.

Activation of BMDCs

BMDCs were harvested from the femur of female C57BL/6 mice and cultured in RPMI 1640 medium containing interleukin-4 (IL-4) and granulocyte-macrophage colony stimulating factor (GM-CSF) at 37 °C in a 5% CO_2 atmosphere.[17] The medium was replaced every 48 h. On day 6, samples were added to the cell suspensions, which were then incubated for 24 h. Then, BMDCs were labelled with dye-conjugated antibodies (anti-CD11c, anti-CD86 and anti-CD80), and the expression levels of CD80 and CD86 were measured by flow cytometry. Meanwhile, the cell supernatant was collected and analyzed to quantify the levels of IFN-β.

Western blotting assay

To assess whether the NPs could activate the STING pathway, BMDCs were incubated with PBS, OVA, OVA + Mn (free OVA physically mixed with Mn^{2+}), OVA@HZIF, and OVA@HZIF-Mn with the same concentration of OVA (20 μg mL^{-1}) at 37 °C in a 5% CO_2 atmosphere for 24 h. After the cells were lysed, we separated the same amounts of proteins using sodium dodecyl sulfate polyacrylamide gel electrophoresis (SDS-PAGE) and transferred them to polyvinylidene difluoride (PVDF) membranes. We performed western blotting analysis using PVDF membranes incubated with antibodies (*i.e.*, β-actin, TBK1, phosphorylated TBK1, STING, and phosphorylated STING).

ELISAs

BMDCs cells were seeded into 24-well plates at a density of 5×10^4 cells at 37 °C in a 5% CO_2 atmosphere overnight and then incubated with PBS, OVA, OVA + Mn, OVA@HZIF, and OVA@HZIF-Mn with the same concentration of OVA (20 μg mL^{-1}) for 24 h. Then, the cells were transferred from the culture plates into centrifuge tubes and centrifuged at 2000*g* for 20 min at 4 °C. The supernatant was analyzed using an ELISA kit to quantify the levels of IFN-β.

Animal studies

Females C57BL/6 mice were obtained from Vital River Laboratory Animal Technology Co., Ltd (China). All animal procedures were performed in accordance with the Guidelines for Care and Use of Laboratory Animals of Shandong First Medical University & Shandong Academy of Medical Sciences and experiments were approved by the Animal Ethics Committee of Shandong First Medical University (NO. W202211090261). To construct the tumor model, the cultured B16F10-OVA cells were prepared into a cell suspension with a density of 2×10^7 mL^{-1}, and 100 μL of the cell suspension was injected into the flank of each mouse to establish a subcutaneous tumor-bearing mouse model. Tumor volume was calculated using $V = 1/2 \times \text{length} \times \text{width}$.[2]

In vivo therapeutic effect

When the tumor volume reached 50 mm^3, the mice were randomly grouped. Then, 100 μL of PBS, OVA + Mn (free OVA physically mixed with Mn^{2+}), OVA@HZIF, and OVA@HZIF-Mn were administered to the tumor-bearing mice by intramuscular injection on days 9, 13, 17, and 21, with the same OVA content of 50 μg. The body weight and tumor volume of the mice were measured every 2 days after injection of the samples. Based on the animal protocol, mouse death was recorded when the tumor volume reached 1500 mm^3. After cessation of treatment, blood was collected, and the serum was isolated and measured to evaluate the biosafety. Furthermore, the organs of mice were collected and stained with hematoxylin and eosin (H&E) for histopathological analysis.

Antitumor immunity *in vivo*

To examine DC maturation *in vivo*, the inguinal lymph nodes of B16F10-OVA tumor-bearing mice were ground to generate lymphocyte single cells. After staining with dye-labelled antibodies (anti-CD11c, anti-CD80, and anti-CD86), the DC cells were measured by flow cytometry. To investigate immune activation and immune memory in the spleen, spleen lymphocytes were generated and stained with dye-labelled antibodies (anti-CD3, anti-CD4, and anti-CD8). Then, spleen lymphocytes were analyzed by flow cytometry. Next, tumors were isolated, homogenized, and digested to obtain single cells. After staining with dye-labelled antibodies, the infiltration of $CD8^+$ T cells ($CD3^+CD8^+$) and $CD4^+$ T cells ($CD3^+CD4^+$) in tumors was measured by flow cytometry.

Statistical analysis

All data are presented as the mean or mean ± standard deviation. A two-tailed Student's *t*-test was used to calculate the significance of the comparisons between two groups. For multiple comparisons, one- or two-way ANOVA with Tukey's or Sidak's multiple comparison test was adopted by GraphPad Prism. $P < 0.05$ was considered as statistically significant.

Author contributions

Y. Z. wrote the manuscript with the help of G. Z. and F. X. conceived the project and wrote, reviewed, and edited the manuscript. Y. Z. and R. S. carried out most of the experiments and analyzed data. Z. Z. contributed to the establishment of the protocols for the synthesis of NPs. Y. H., W. N. and X. D. participated in the *in vivo* experiments. Y. H., W. N. and X. D. were involved in the study design and manuscript preparation. G. Z., F. X. and J. J. were in charge of the study design, work organization/supervision, manuscript review, and funding acquisition. All authors have read and agreed to the published version of the manuscript.

Conflicts of interest

There are no conflicts to declare.

Acknowledgements

This work was supported by Natural Science Foundation of Shandong Province (ZR2023MB081 and ZR2021RH255), Project for Scientific Research Innovation Team of Young Scholars in Colleges and Universities of Shandong Province (No. 2022KJ196), and Technology SMEs Innovation Capability Improvement Project of Shandong Province (2022TSGC2050).

Notes and references

1 S. A. Rosenberg, J. C. Yang and N. P. Restifo, *Nat. Med.*, 2004, **10**, 909–915.
2 J. Xu, J. Lv, Q. Zhuang, Z. Yang, Z. Cao, L. Xu, P. Pei, C. Wang, H. Wu, Z. Dong, Y. Chao, C. Wang, K. Yang, R. Peng, Y. Cheng and Z. Liu, *Nat. Nanotechnol.*, 2020, **15**, 1043–1052.
3 D. Qiao, Y. Chen and L. Liu, *Biomaterials*, 2021, **269**, 120674.
4 Z. Hu, P. A. Ott and C. J. Wu, *Nat. Rev. Immunol.*, 2018, **18**, 168–182.
5 Y. Lu, Y. Shi and J. You, *J. Controlled Release*, 2022, **341**, 184–205.
6 R. Kuai, L. J. Ochyl, K. S. Bahjat, A. Schwendeman and J. J. Moon, *Nat. Mater.*, 2017, **16**, 489–496.
7 B. Lou, A. De Beuckelaer, E. Boonstra, D. Li, B. G. De Geest, S. De Koker, E. Mastrobattista and W. E. Hennink, *J. Controlled Release*, 2019, **293**, 48–62.
8 S. Wu, Y. Xia, Y. Hu and G. Ma, *Adv. Drug Delivery Rev.*, 2021, **176**, 113871.
9 D. J. Irvine, M. C. Hanson, K. Rakhra and T. Tokatlian, *Chem. Rev.*, 2015, **115**, 11109–11146.
10 D. Cao, W. Guo, C. Cai, J. Tang, W. Rao, Y. Wang, Y. Wang, L. Yu and J. Ding, *Adv. Funct. Mater.*, 2022, **32**, 2206084.
11 Y. Du, T. Song, J. Wu, X. D. Gao, G. Ma, Y. Liu and Y. Xia, *Biomaterials*, 2021, **280**, 121313.

12 Z. L. Gao, W. Xu, S. J. Zheng, Q. J. Duan, R. Liu and J. Z. Du, *Nano Lett.*, 2023, **23**, 1904–1913.
13 D. Liu, B. Deng, Z. Liu, B. Ma, X. Leng, D. Kong, T. Ji and L. Liu, *Nano Lett.*, 2021, **21**, 3965–3973.
14 R. Zhang, L. Tang, Y. Wang, Y. Tian, S. Wu, B. Zhou, C. Dong, B. Zhao, Y. Yang, D. Xie and L. Yang, *Adv. Sci.*, 2023, e2300116.
15 X. Ji, L. Ge, C. Liu, Z. Tang, Y. Xiao, W. Chen, Z. Lei, W. Gao, S. Blake, D. De, B. Shi, X. Zeng, N. Kong, X. Zhang and W. Tao, *Nat. Commun.*, 2021, **12**, 1124.
16 G. Chong, J. Zang, Y. Han, R. Su, N. Weeranoppanant, H. Dong and Y. Li, *Nano Res.*, 2021, **14**, 1244–1259.
17 M. A. Luzuriaga, F. C. Herbert, O. R. Brohlin, J. Gadhvi, T. Howlett, A. Shahrivarkevishahi, Y. H. Wijesundara, S. Venkitapathi, K. Veera, R. Ehrman, C. E. Benjamin, S. Popal, M. D. Burton, M. A. Ingersoll, N. J. De Nisco and J. J. Gassensmith, *ACS Nano*, 2021, **15**, 17426–17438.
18 X. Li, X. Wang, A. Ito and N. M. Tsuji, *Nat. Commun.*, 2020, **11**, 3858.
19 G. Zhang, X. Fu, H. Sun, P. Zhang, S. Zhai, J. Hao, J. Cui and M. Hu, *ACS Appl. Mater. Interfaces*, 2021, **13**, 13978–13989.
20 À. Ruyra, A. Yazdi, J. Espín, A. Carné-Sánchez, N. Roher, J. Lorenzo, I. Imaz and D. Maspoch, *Chemistry*, 2015, **21**, 2508–2518.
21 R. Ettlinger, U. Lächelt, R. Gref, P. Horcajada, T. Lammers, C. Serre, P. Couvreur, R. E. Morris and S. Wuttke, *Chem. Soc. Rev.*, 2022, **51**, 464–484.
22 M. Hu, Y. Ju, K. Liang, T. Suma, J. Cui and F. Caruso, *Adv. Funct. Mater.*, 2016, **26**, 5827–5834.
23 C. Wang, R. Zhang, X. Wei, M. Lv and Z. Jiang, *Adv. Immunol.*, 2020, **145**, 187–241.
24 C. Wang, Y. Guan, M. Lv, R. Zhang, Z. Guo, X. Wei, X. Du, J. Yang, T. Li, Y. Wan, X. Su, X. Huang and Z. Jiang, *Immunity*, 2018, **48**, 675–687.e7.
25 Y. Takagi, A. Okada, K. Sando, M. Wasa, H. Yoshida and N. Hirabuki, *Am. J. Clin. Nutr.*, 2002, **75**, 112–118.
26 N. Wang, G. Zhang, H. Sun, Y. Tian, J. Hao and J. Cui, *Chem. Mater.*, 2021, **33**, 4057–4066.